Check for updates

Diversity at the nanoscale: laser-oxidation of single-layer graphene affects Fmoc-phenylalanine surface-mediated self-assembly†

Johanna Schirmer, [ID] [a] Romain Chevigny, [ID] [a] Aleksei Emelianov, [ID] [a] Eero Hulkko, [ab] Andreas Johansson, [ID] [ac] Pasi Myllyperkiö, [ID] [a] Efstratios D. Sitsanidis, [ID] *[a] Maija Nissinen [ID] *[a] and Mika Pettersson [ID] *[a]

We report the effects of a laser-oxidized single layer graphene (SLG) surface on the self-assembly of amphiphilic gelator *N*-fluorenylmethoxycarbonyl-L-phenylalanine (Fmoc-Phe) towards an gel–SLG interface. Laser oxidation modulates the levels of hydrophobicity/hydrophilicity on the SLG surface. Atomic force, scanning electron, helium ion and scattering scanning nearfield optical microscopies (AFM, SEM, HIM, s-SNOM) were employed to assess the effects of surface properties on the secondary and tertiary organization of the formed Fmoc-Phe fibres at the SLG–gel interface. S-SNOM shows sheet-like secondary structures on both hydrophobic/hydrophilic areas of SLG and helical or disordered structures mainly on the hydrophilic oxidized surface. The gel network heterogeneity on pristine graphene was observed at the scale of single fibres by s-SNOM, demonstrating its power as a unique tool to study supramolecular assemblies and interfaces at nanoscale. Our findings underline the sensitivity of assembled structures to surface properties, while our characterization approach is a step forward in assessing surface–gel interfaces for the development of bionic devices.

Introduction

Advances in neuron–machine connections at micro- and nano-scale have given new hope in repairing brain and nervous system damage.[1–4] A key part of such connections is the interface between the neural tissue and the bioelectronic device, as it should support neuron viability and functionality while preserving the electronic properties of the device. With its exceptional mechanical stability and electronic properties, graphene is a promising candidate for constructing neuron–machine interfaces, as it has been shown to record neural activity successfully.[5–7] In our previous studies, we employed laser-oxidation[8] to modulate the properties of single-layer graphene (SLG) towards bioinspired surfaces, functionalized with proteins.[9] The two-photon oxidation process with a femtosecond laser in ambient atmosphere

introduced patterned hydroxyl and epoxide groups on the graphene surface, while the carbon network remained intact (Fig. 1A).[8,10]

Besides the desired surface properties, the neurons must remain viable and functional, attach to the artificial device, and interact with it to achieve functional bionic devices. In living tissue, neurons build their own extracellular matrix (ECM), an extensive network of proteins such as fibrous proteins, glyco-proteins, and proteoglycans,[11] which supports the cells and regulates intracellular communication. However, for constructing artificial neuron–machine interfaces, it is crucial to functionalize the surface with a biocompatible substrate material, for example, a supramolecular gel, to mimic the properties of natural ECM. This will enable and support the growth of a three-dimensional (3D) neural network, adjacent to the electronic device, forming a neuron–machine interface.[12–14]

Low molecular weight gels (LMWGs) have gained momentum in the field of biomaterials due to their biocompatibility, easy preparation, structural functionalization, tunability and mechanical properties.[15] In supramolecular gels, the gelator molecules self-assemble hierarchically towards higher order architectures. Initially, molecular recognition events promote the gelators' assembly in one or two dimensions (primary structure), followed by the formation of aggregates such as fibres, ribbons, sheets, and micelles (secondary structure), while the interaction of individual aggregates (tertiary structure)

[a] Department of Chemistry, Nanoscience Center, University of Jyväskylä, P. O. Box 35, FI-40014 JYU, Finland. E-mail: mika.j.pettersson@jyu.fi, maija.nissinen@jyu.fi, efstratios.d.sitsanidis@jyu.fi

[b] Department of Biological and Environmental Sciences, Nanoscience Center, University of Jyväskylä, P. O. Box 35, FI-40014 JYU, Finland

[c] Department of Physics, Nanoscience Center, University of Jyväskylä, P. O. Box 35, FI-40014 JYU, Finland

† Electronic supplementary information (ESI) available: Experimental and computational details, sample optimization, crystal characterization, Raman and nano-FTIR spectra, DFT results. See DOI: https://doi.org/10.1039/d3cp00117b

This journal is © the Owner Societies 2023

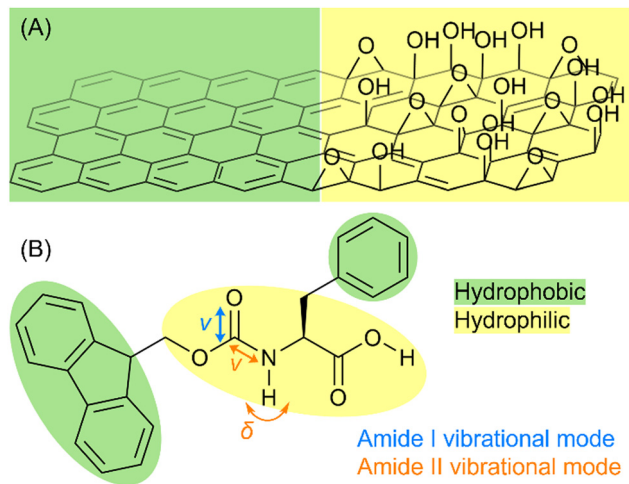*Phys. Chem. Chem. Phys.*, 2023, **25**, 8725–8733 | 8725

Fig. 1 (A) Scheme of laser-oxidized SLG, showing pristine and oxidized areas adjacent to each other. (B) Chemical structure of Fmoc-Phe; the arrows depict vibrations that contribute to the amide I (blue) and amide II (orange) vibrational modes. Stretching vibrations are indicated as ν and bending vibrations as δ. Hydrophobic moieties are highlighted in green, hydrophilic moieties in yellow.

determines the gel's formation.[16,17] The micro- and macroscopic properties of bulk materials can be tuned by modifying the chemical structure of the gelator, the concentration and/or the solvent (i.e., buffer solutions, pH).[18–20] However, at a machine–tissue interface, the soft hydrogel is in direct contact with the tissue and the device's surface, meaning that surface-mediated self-assembly phenomena have an immediate effect on the formation and corresponding properties of supramolecular gels.[21–25] For example, interactions between the monomers and the surface can boost or decelerate the fibrillation of amyloid-β peptides.[26,27] Additionally, the hydrophobicity/hydrophilicity of the surface plays a significant role in surface-mediated self-assembly, affecting the fibre's diameter, aggregation and/or Young's modulus of the formed gels.[21,22] Further to this, increased surface roughness has been found to decelerate and finally inhibit the fibrillation of an amyloid-β peptide.[28] A surface–gel system may be probed at a small volume. For example, Yang et al.[25] observed changes in the viscosity and structure of a supramolecular gel drop (350 μl) on a photo-patterned surface with different physical properties.

The analysis of a supramolecular gel–surface interface is mainly confined to microscopic and X-ray techniques: The physical properties and morphology of the gel's network have been studied by atomic force (AFM) and (cryo-)scanning electron (SEM) microscopy.[21,23,24,29] To analyse the secondary and tertiary structure of the gels, grazing-incidence wide and small angle X-ray scattering[22] and grazing-incidence X-ray diffraction[25] have been employed. A relatively new technique for surface analysis is scattering scanning near-field optical microscopy (s-SNOM), which combines AFM in tapping mode and an infrared (IR) laser that points at the AFM tip apex. When interacting with the sample, the near-field (NF) signal of the tip is altered and elucidates the absorptive properties of the sample in the spectral region of the incident laser.[30–33] With a spatial resolution down

to 6 nm for visible light and near IR absorption[34] and 1 nm for tip-enhanced Raman spectroscopy,[35] or even down to atomic resolution,[36] it is possible to obtain locally defined absorptive properties of a material in the form of nano-FTIR/Raman spectra and absorption/reflectivity images. The structure of a supramolecular gel can be analysed at the nanoscale, and valuable information on the heterogeneity and distribution of the gel material on a surface can be received.

In this study, we assessed the surface-mediated self-assembly of model gelator N-fluorenylmethoxycarbonyl-L-phenylalanine (Fmoc-Phe) on pristine (prG) and laser-oxidized (oxG) graphene (Fig. 1). The bulk gels of Fmoc-Phe and its derivatives have been extensively studied.[19,20,37–39] Due to the anionic and amphiphilic nature of the amino acid, both electrostatic interactions and hydrophobic effects promote self-assembly. Gelation is therefore sensitive to pH changes and the presence of ions.[20] Additionally, the aromaticity, hydrophobicity and spatial flexibility of the phenyl ring affect the properties of the gel.[19,20] Fmoc-protected or Phe-based gelators tend to form β-sheet-like structures[40,41] and the crystal structure of Fmoc-Phe shows a unidirectional, sheet-like assembly of the molecules.[38] A recent study, however, demonstrates that gel fibres and crystals do not necessarily have similar structures, as the size and shape of the sample container affect the assembly event.[42] In contrast to bulk gels, the structure of Fmoc-Phe fibres on a surface is difficult to predict, as the effect of surface properties on the secondary structure remains an open question.

S-SNOM, AFM, SEM and helium ion microscopy (HIM) allowed us to study the effects of distinct surface properties on the surface-mediated self-assembly of the amino acid. We identified different secondary structures of the fibres by nano-FTIR spectroscopy and nanoscale mid-IR (MIR) imaging. At the same time, we demonstrated the modulation of the Fmoc-Phe self-assembly by laser-oxidation and hence the effects of SLG's different levels of hydrophobicity/hydrophilicity. Overall, a structurally heterogeneous fibrous network of Fmoc-Phe is formed on both surfaces, prG and oxG.

Results and discussion

Surface effects on gel morphology and fibre dimensions

Surface-mediated self-assembly can be modulated depending on the physicochemical properties of the surface.[21,25] Here, SLG was patterned with oxidized areas via laser-irradiation, to assess the self-assembly of amphiphilic gelator Fmoc-Phe. The surface consists of hydrophobic/flat prG (R_a = 0.23 nm, where R_a is arithmetic average height[43]) adjacent to hydrophilic/rough oxG (R_a = 0.33 nm).[8] Ten parallel rectangular patterns were irradiated (40 μm × 400 μm in size) and arranged approximately 160 μm apart, creating an alternating motif of oxG and prG (Fig. 2). An Fmoc-Phe solution in phosphate buffer (PBS) was then added on the graphene surface and allowed to gel overnight, followed by freezing and lyophilization of the gel–SLG interface prior analysis. A detailed description of the experimental and sample preparation procedures can be found in the ESI† (Sections S1–S4).
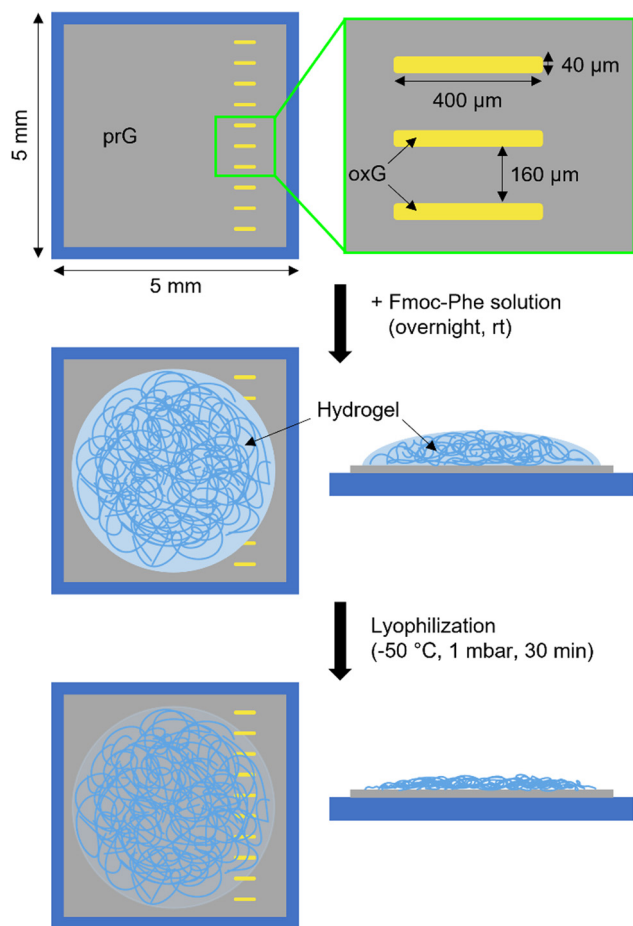
8726 | *Phys. Chem. Chem. Phys.*, 2023, **25**, 8725–8733

This journal is © the Owner Societies 2023

Fig. 2 Schematic depiction of the SLG sample geometry and gel–SLG interface preparation. Yellow rectangular patterns represent irradiated, laser-oxidized graphene and the Si/SiO₂ substrate is depicted in blue.
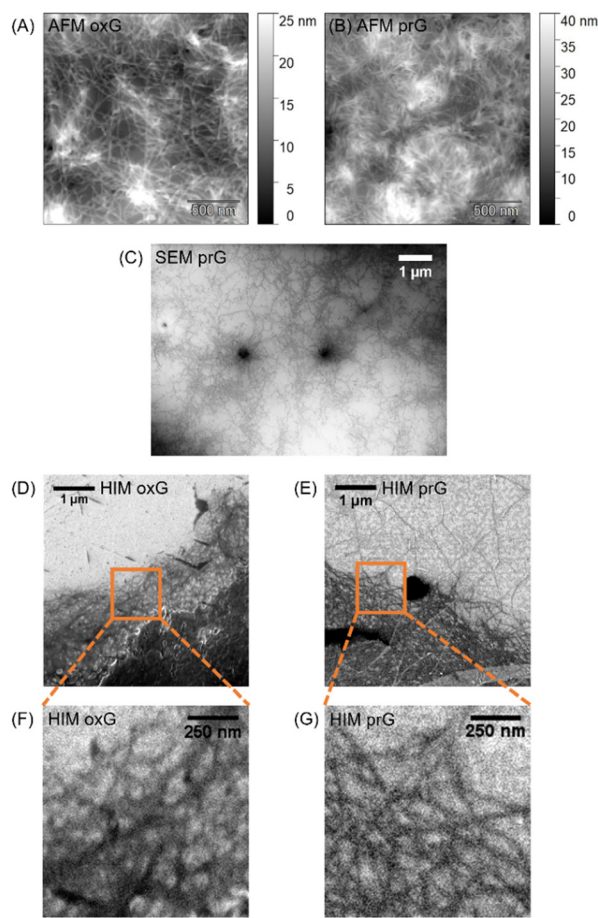

Fig. 3 Microscopic analysis of the Fmoc-Phe fibres on oxG and prG: AFM images on oxG (A) and prG (B); SEM image on prG showing two nucleation sites (C); HIM images of the Fmoc-Phe gel edge on oxG (D) and prG (E) and corresponding magnified images (F) and (G), respectively, indicated by the orange rectangles.

AFM, SEM and HIM imaging were employed to analyse the gel morphology and fibres' dimensions (Section S1, ESI†). The fibres in supramolecular gels are larger architectures formed by the organization of many fibrils. An entangled fibrous network was visible in the AFM topographic images on both prG and oxG surfaces (Fig. 3A and B). Single fibres entangle into thicker bundles, creating a dense network. The fibre thickness was measured using the AFM images, as an average of 100 single fibres on each surface. The average thickness of the fibres t on the two surfaces is almost identical ($t_{prG} = 2.0 \pm 1.0$ nm, $t_{oxG} = 2.3 \pm 1.1$ nm, one-way ANOVA, $p < 0.001$), which indicates no significant effect of surface properties on the size of the Fmoc-Phe fibres.

SEM imaging of the Fmoc-Phe xerogel (dried gel) on prG (Fig. 3C) showed fibres growing from spherulites (dark spots), consistent with previous observations on Phe-based gels.[24,44] HIM imaging, at the edges of the supramolecular network, on both oxG and prG (Fig. 3D–G) revealed a slightly different appearance of the fibres in contrast to the AFM images, which were taken at the center of the gel network. On oxG, the fibres appear curved in the HIM images, whereas straight on prG. During the sample preparation (Fig. 2), the fibre density was lower at the edges of the gel. Fibres at the edges grow near the surface and may therefore be affected by the surface properties to a greater extent than fibres in the center of the gel network (AFM images).[21] The observed difference in fibre morphology suggests that the hydrophobic/hydrophilic differences upon the SLG surface affect the tertiary organization level (fibril–fibril interaction) of Fmoc-Phe in the proximity of the surface.

Surface effects on the secondary organization level

To investigate the self-assembly and molecular interactions of Fmoc-Phe on prG and oxG surfaces at the nanoscale (secondary organization level), the gel–SLG interface was studied by s-SNOM (Section S1, ESI†). Singh et al.[20] have reported that both hydrogen bonding and hydrophobic stacking interactions contribute to the self-assembly of Fmoc-Phe, which carries a negative net charge at pH 7.4. IR, ultraviolet-visible, circular dichroism, and nuclear magnetic resonance spectroscopy revealed a heterogeneous secondary structure, consisting of stacked molecules (different polymorphs). The fluorenyl group appears to stack with the phenyl ring while the carbamate group is involved in hydrogen bonding. However, these

observations derive from the bulk gel, meaning that the spectroscopic data of the whole bulk material were averaged. Here, we studied the absorptive properties of the fibres on the scale of single fibres and fibre bundles (nano- and microscale). We hypothesized that potential effects of the graphitic surface on the secondary structure of Fmoc-Phe could be observable in the nano-FTIR spectrum. Additionally, we suggested that the polymorphic nature of the bulk gel, as previously reported,[20] would be confirmed by MIR imaging at different frequencies.

Secondary structure analysis. Initially, nano-FTIR spectra were taken from five oxG and six prG positions on the gel–SLG interface (Section S5, ESI†). Each spectrum was normalized to the corresponding background (oxG or prG, respectively) to eliminate the contribution of the graphene surface. The optical phase spectrum (referred to as "nano-FTIR spectrum") corresponds to the absorptive properties of the fibres inside the near-field.[33] We analysed the 3rd harmonic of the cantilever oscillation as it yields detailed spectral features at an adequate signal-to-noise ratio. We focused on the frequency range between 1500 cm^{-1} and 1750 cm^{-1}, corresponding to the carbonyl and amide vibrations. The amide II band appears approximately at 1550 cm^{-1} as a combination of the N–H bending and C–N stretching vibration (Fig. 1B). The absorption band(s) between 1600 cm^{-1} and 1700 cm^{-1} (amide I region), arise from the C$=$O stretching vibration and are immediately related to the secondary structure of the gel sample.[45] For protein samples, it has been reported that the amide I band shifts and/or splits depending on the secondary structures[45,46] and common secondary structures like α-helices and β-sheets, forming via hydrogen bonding of the amide backbone, absorb at certain frequencies. According to Barth,[45] α-helices show one main absorption approximately at 1655 cm^{-1}. However, disordered structures absorb at a similar frequency, while β-sheets give rise to two absorption bands in the amide I region ($\leq$1640 cm^{-1} and $\geq$1680 cm^{-1}), resulting from the transition dipole coupling of the carbonyl groups. In a single molecule, the carbonyl C$=$O vibration shows only one band. When coupled with another C$=$O oscillator, at a β-sheet conformation, the excitation leads to exciton splitting and splitting of the absorption band.[46] The difference between the two bands depends on the strength of the IR absorption (stronger absorption = larger splitting) and the distance and orientation of the two oscillators to each other. During the self-assembly of the amino acid-based gelators, the molecules arrange into similar secondary structures via hydrogen bonding of the amide group(s). Therefore, changes in the molecular arrangement due to different surface properties are expected to be observable in the amide I region of the nano-FTIR spectra. It is of note that band positions may shift a few wavenumbers when comparing transmission FTIR and nano-FTIR spectra.[47]

Fig. 4 shows the AFM images of the Fmoc-Phe fibres on oxG and prG and one nano-FTIR spectrum from each surface area. Several overlapping bands appeared in the amide I and II regions. Spectra of the same surface area showed mostly similar band positions (Table 1 and Fig. S4, ESI†). However, there were noticeable shifts among the gel–oxG and –prG interfaces. Fmoc-Phe fibres showed two absorption bands on both surfaces
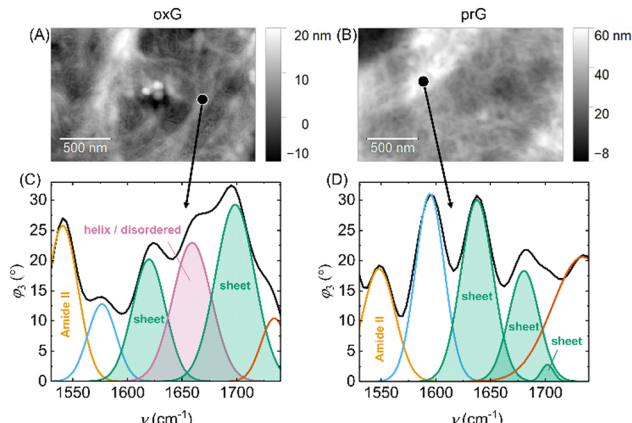

Fig. 4 Nano-FTIR study of Fmoc-Phe fibre bundles on oxG and prG: AFM topographic images of Fmoc-Phe fibres on (A) oxG and (B) prG; corresponding deconvoluted nano-FTIR spectra in the amide I and II regions (C and D). The exact position of each spectrum is highlighted with a black spot in the corresponding AFM image. The filled bands in the Amide I region show the assigned secondary structure elements.

at frequencies typical for β-sheet structures (oxG: 1618 cm^{-1} and 1699 cm^{-1}, prG: 1640 cm^{-1} and 1683 cm^{-1}). The bands' centres were further apart on oxG (distance: 81 cm^{-1}) than on prG (distance: 43 cm^{-1}). Since the strength of the IR absorption should be similar for all Fmoc-Phe molecules, our results suggest that the orientation and/or distance of C$=$O groups change between sheet-like assemblies on oxG or prG, leading to different couplings. On oxG, the fibres additionally gave rise to a band at 1657 cm^{-1}, suggesting the presence of α-helices or disordered structures.[46] Interestingly, this band was absent in 67% of the spectra of Fmoc-Phe on prG. Therefore, these findings indicate a connection between the secondary structure of the fibres and the surface properties (differences in hydrophobicity/hydrophilicity) of oxG and prG.

To investigate the proportion of different types of secondary structures over the oxG and prG surfaces, the areas of the bands, assigned to secondary structures (highlighted in Fig. 4C and D for the sample spectra), were compared at each spectrum. To obtain a quantitative comparison profile, the input of each secondary structure was calculated (Section S1, ESI†). The sum

Table 1 Band positions and their standard deviation derived from the second derivative of each spectrum from Fig. S4E and F, ESI. In parenthesis behind the number, the abundance of the respective band in the whole sample N is shown ($N_{oxG} = 5$, $N_{prG} = 6$). Bold numbers indicate bands that appear in at least 80% of the samples. A secondary structure was assigned to absorbance bands in the Amide I region

Peak positions oxG	Peak positions prG	Assigned secondary structure
1546 ± 5 (5/5)	**1558 ± 5 (6/6)**	
1578 ± 1 (3/5)		
1598 (1/5)	**1600 ± 4 (6/6)**	
1618 ± 3 (5/5)		Sheet
	1640 ± 4 (5/6)	Sheet
1657 ± 1 (5/5)	1656 ± 0 (2/6)	Helix/disordered
	1683 ± 6 (6/6)	Sheet
1699 ± 2 (5/5)	1707 ± 3 (4/6)	Sheet

8728 | *Phys. Chem. Chem. Phys.*, 2023, **25**, 8725–8733

This journal is © the Owner Societies 2023

Table 2 Input of sheet and helix/disordered structures for nano-FTIR spectra of Fmoc-Phe fibre bundles on oxG and prG

#Spectrum	Input sheet (%)	Input helix/disordered (%)
oxG		
1	87	13
2	74	26
3	52	48
4	62	38
5	67	33
prG		
1	100	0
2	100	0
3	87	13
4	57	43
5	100	0
6	100	0

of areas of all bands assigned to secondary structures was set to 100% in each spectrum. Although this approach is not rigorously accurate as it overlooks the differences between oscillator strengths for different vibrations, it allows to compare proportions of different structures between different areas. The inputs are presented in Table 2. As described above, all spectra on oxG showed absorption bands at both β-sheet and α-helix/disordered structure frequencies. However, the inputs varied from 52% to 87% for β-sheets and 13% to 48% for α-helix/disordered structures. This indicates a heterogeneous fibrous network, which supports the presence of different polymorphs as reported by Singh *et al.* in bulk gels.[20] On prG, most spectra showed a network solely consisting of β-sheets. Though, in two positions, different amounts of α-helix/disordered structures were found (13% and 43%). Possible reasons for the appearance of this band on prG are: (i) the spectra were taken at positions near the oxidized areas (Fig. S4, prG spectrum 1–3, ESI†). Since prG and oxG are adjacent (Fig. 1B) and Fmoc-Phe fibres can be several micrometres long, it is possible that some cross the boundary between the two surfaces. (ii) The dried sample transforms the 3D network to a 2D (Fig. 2). This could lead to the displacement of the fibres from their original location in the 3D network. However, the trend of solely β-sheet structures on prG is strong, and there is a clear difference between the inputs of secondary structures, depending on the surface oxidation.

Surface–monomer interactions. At the gel–SLG interface system, the differences in hydrophobicity/hydrophilicity are expected to result in secondary structure alterations of Fmoc-Phe. A previous study reported a cytidine-based gelator which formed a gel on hydrophobic/hydrophilic surfaces.[21] The material had a different Young's modulus and diameter of fibres depending on the surface's hydrophobicity. In addition, different amyloid peptides form fibrils preferably on hydrophobic surfaces,[26,29] suggesting that distinct electrostatic interactions and hydrophobic effects between the surface and the monomers are responsible for the assembly event. Such effects apply to relatively few molecules adsorbed on the surface. The monomer–surface interactions could affect the self-assembly process alongside an entire fibre if its formation starts from a nucleation point at the surface. Depending on the spatial orientation of the molecules adsorbed on the surface, *i.e.* the functional groups interacting with the surface, different functional groups of the molecule point towards the monomer solution. In this way, distinct nucleation points are created. During the surface-mediated self-assembly, the subsequent molecules interact with different functional groups, depending on the spatial orientation of the monomer adsorbed on the surface. The distinct interactions could lead to distinct secondary structures. Regarding Fmoc-Phe, the self-assembly may start *via* π–π stacking or hydrogen bonding. The surface hydrophobicity/hydrophilicity could affect the preferred type of interaction.

To investigate the interactions between the two surfaces (oxG and prG) and the Fmoc-Phe monomer, we performed density functional theory (DFT) calculations to obtain the adsorption energies (E_{ads}) of the Fmoc-Phe monomer on oxG and prG, respectively (Section S6, ESI†). By varying the distance and orientation of Fmoc-Phe towards the two surfaces, we aimed to identify the most stable configurations. Though the model is calculated under a vacuum state, it gives insight into the driving forces of molecular adsorption onto the surfaces. On oxG, the Fmoc-Phe monomer tends to orient its polar groups towards the oxygen-containing groups of the surface (Fig. 5A–D). The distances between 2.2 Å and 3.0 Å (Table S2, ESI†) and E_{ads} between −0.63 eV and −0.77 eV indicate physisorption and the formation of hydrogen bonds. Especially, the carboxylic moiety (COOH) of Phe is involved in hydrogen bonding. The reason for the surface–COOH interaction is likely the sterically less hindered position of COOH compared to the amide group, which is sterically shielded by the Fmoc and phenyl aromatic moieties and COOH. When Fmoc-Phe adsorbs on the surface in these orientations (Fig. 5A–D), the aromatic moieties point towards the gelator solution and could generate a nucleation site for further self-assembly *via* π–π stacking.

On the prG surface, the adsorption of Fmoc-Phe leads partly to different orientations (Fig. 5E–H). Here, the aromatic moieties play the main role during the DFT structure optimization. With surface–monomer distances between 2.7 Å and 3.9 Å (Table S2, ESI†) and E_{ads} between −0.62 eV and −0.89 eV, non-covalent interactions such as π–π stacking may contribute to the physisorption. Indeed, parallel π–π stacking is observed between prG and Fmoc or the phenyl ring (Fig. 5G and H, respectively). By occupying the aromatic moieties of Fmoc-Phe in surface–monomer interactions, the hydrophilic amide and COOH groups could play a more significant role in initiating the self-assembly of Fmoc-Phe beyond the surface. While, for example, structures D (oxG) and G (prG) are different regarding the orientation and adsorption-involving groups, structures A and B on oxG appear similar to structures E and F on prG, respectively. The observation of similar and distinct adsorption orientations of Fmoc-Phe on both surfaces in DFT results complements the obtained nano-FTIR results: The spectra of the self-assembled structures on oxG and prG show both similar and distinct bands. Thus, it is probable that the self-assembly of Fmoc-Phe on prG and oxG is a surface-mediated process.

Heterogeneity of the fibrous network. The nano-FTIR spectra were recorded at the positions of fibre bundles and overlaying

This journal is © the Owner Societies 2023

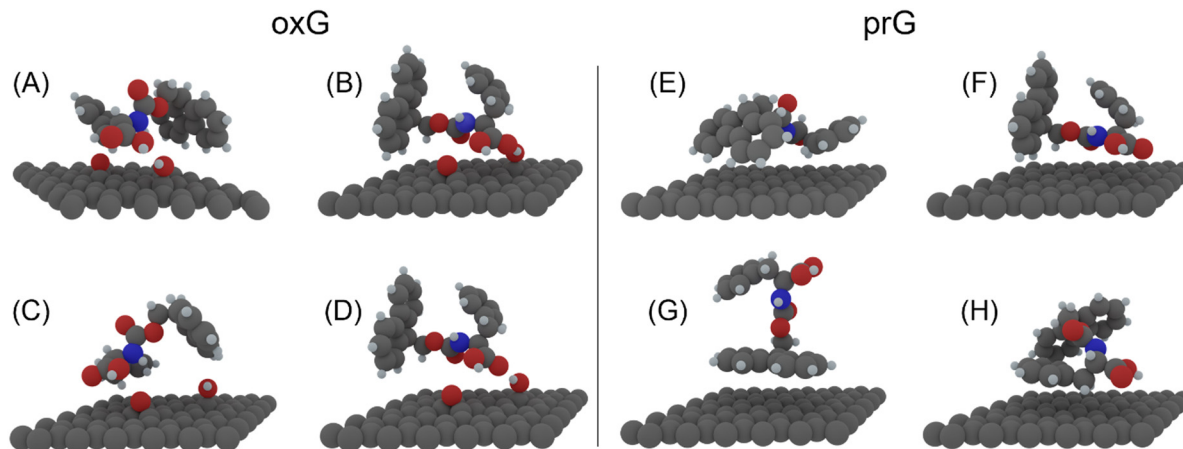*Phys. Chem. Chem. Phys.*, 2023, **25**, 8725–8733 | 8729

Fig. 5 Adsorption of Fmoc-Phe on oxG (A–D) and prG (E–H) surfaces (DFT study). Four of the energetically most stable structures are shown for each surface. The corresponding adsorption energies are (A) −0.73 eV, (B) −0.77 eV, (C) −0.63 eV, (D) −0.65 eV, (E) −0.89 eV, (F) −0.66 eV, (G) −0.63 eV and (H) −0.62 eV.

fibres to obtain an adequate NF signal. To investigate the potential polymorphic forms of the gelator in single fibres, a series of MIR phase images were obtained of the Fmoc-Phe fibres on prG. A fibrous network of low density was selected, at the edge of the gel, to achieve adequate contrast in the images. The imaging frequencies were selected to cover the amide II (1546 cm^{-1}), amide I (1600 cm^{-1}, 1645 cm^{-1}, 1672 cm^{-1} and 1699 cm^{-1}) and off-amide vibrations (1720 cm^{-1}) (Fig. 6A). The topography and corresponding optical phase images are presented in Fig. 6B–H. The three wide lines were visible in all optical phase images, while not in the topography image (Fig. 6H). These likely originate from defects or wrinkles of the graphene monolayer, which were observed in the NF signal.[48] Here, the signal overlapped with the signal of fibres deposited in this area. The highest contrast between prG surface and the fibre network was visible at frequencies of the β-sheet region (1645 cm^{-1}, 1672 cm^{-1} and 1699 cm^{-1}), underpinning the relevance of sheet-like secondary structures of Fmoc-Phe on prG. Another frequency revealing a high contrast was that of 1600 cm^{-1}. This behaviour correlates with the intense band around 1600 cm^{-1} in all the recorded spectra on prG (for example, Fig. 6A). The aromatic C–C stretching of the Fmoc and phenyl moieties could give rise to this band.[49,50]

Overall, the detected vibrational modes occurred heterogeneously throughout the fibre network, as shown by the varying intensity of the phase shift in Fig. 6C–H. To investigate if the NF phase change was caused by height variations and the accompanying varying number of molecules, a model fibre was analyzed in detail (Fig. 6I, orange dashed line). The cross-sections from the topography image and the optical phase images at 1645 cm^{-1} and 1699 cm^{-1} are shown in Fig. 6J. The phase profiles do not follow the height profile linearly or inversely throughout the cross-section. The two optical phase signals have a similar magnitude in the yellow (entangled fibres) and blue highlighted parts (single fibre) of the profile. In contrast, the height of the entangled fibres is bigger compared to the single fibre. Thus, the difference in optical phase signal intensity probably did not

originate from height variations but was due to differences, for example, in the secondary structure of the material.

To investigate trends in absorption for single and entangled fibres, all imaged frequencies were compared at specific location points on the fibres (symbols in Fig. 6I). The optical phase signals of these points were plotted against the imaging frequency (Fig. 6K), leading to an optical phase profile. For each data point in plot Fig. 6K, the optical phase values of 5 pixels were averaged. The orange and blue plots (Fig. 6K) correspond to the two single fibres, which form a coiled coil formation (represented by the black and green plots in Fig. 6K). The yellow plot shows the signal at a different entanglement point. Each plot has a different shape, meaning the signal profile is different. However, the signal profiles of the black and green plots have a similar shape except for one point (1699 cm^{-1}). The signal profiles of the two entanglement points (Fig. 6I, black and yellow squares) do not correlate. Also, the signal profiles of the two single fibres have different shapes. Indeed, these findings showcase the heterogeneity of the fibrous network and support previous findings of polymorphic forms in the Fmoc-Phe lyophilized bulk gel.[20] Moreover, our results demonstrate variations of the secondary structure of Fmoc-Phe molecules at a single fibre level.

Conclusions

In summary, we gained insight into the surface-mediated self-assembly process of amphiphilic gelator Fmoc-Phe at the interface of an SLG surface and highlighted the effect of graphene's laser-oxidation on gelation at the secondary and tertiary organization levels. Based on our findings, nano-FTIR can distinguish different secondary structures of supramolecular gels at the nanoscale. The secondary structure of Fmoc-Phe fibres is affected by the laser-oxidation of the SLG surface, which results in different hydrophobic/hydrophilic surface areas. On the hydrophobic prG, sheet-like structures dominate the network,
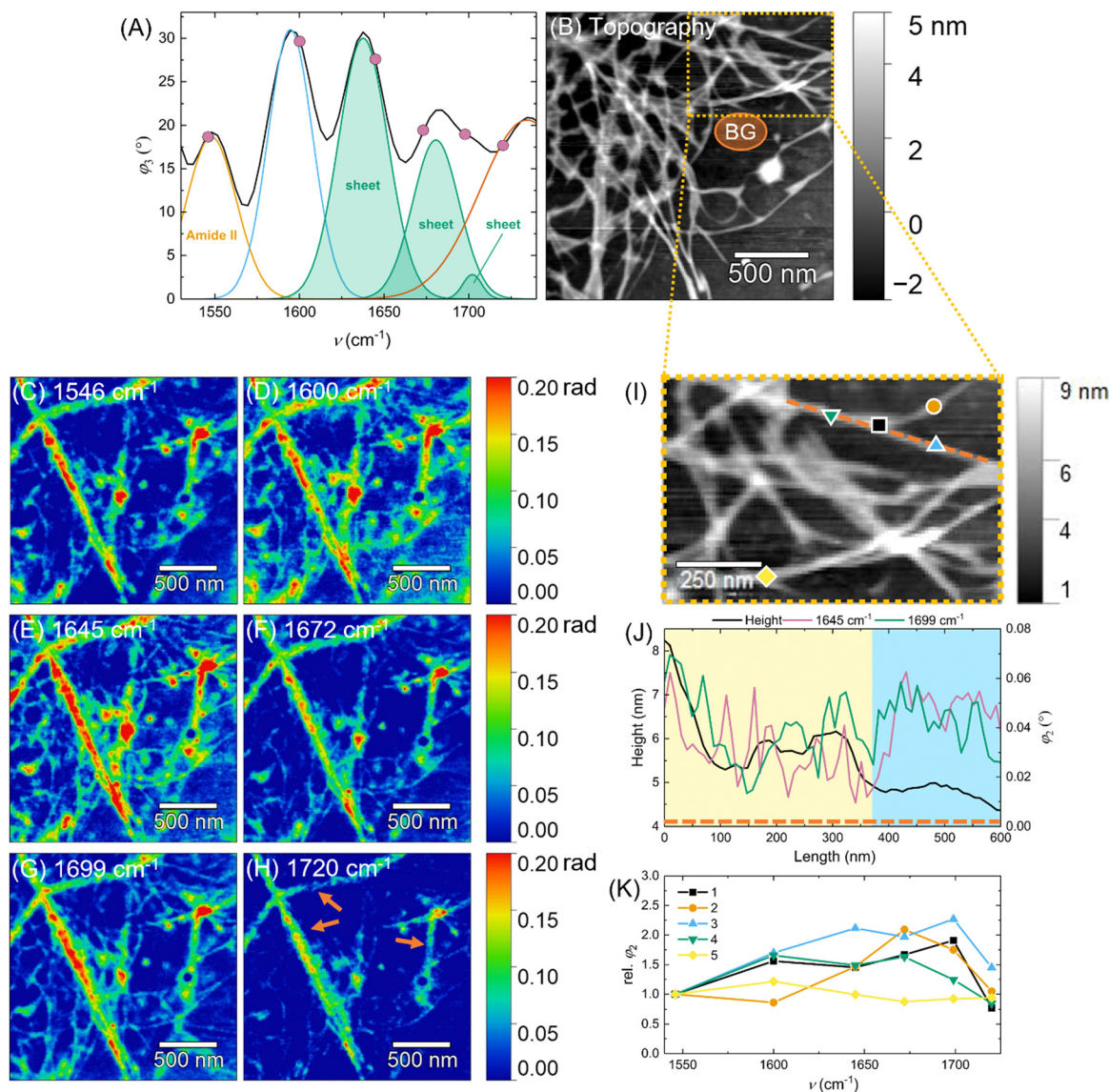
8730 | *Phys. Chem. Chem. Phys.*, 2023, **25**, 8725–8733

This journal is © the Owner Societies 2023

Fig. 6   MIR imaging study of Fmoc–Phe fibres on prG: (A) frequencies of imaging (purple dots) highlighted in a nano-FTIR spectrum of the fibres on prG; (B) AFM topographic image of the fibres on prG. The area highlighted in orange was used as a background in all images; (C–H) corresponding optical phase φ^2 images, the imaging frequency is given in each image; (I) a magnification of image (B); (J) height/intensity profiles corresponding to the orange dashed line in (I). Plots from topography (black), 1645 cm^{-1} (purple) and 1699 cm^{-1} (green); (K) relative phase from each optical phase image at certain points, marked in (I).

while additional helical or disordered structures were observed on hydrophilic oxG. Additionally, laser-oxidation can affect the tertiary organization level (fibril–fibril interactions) of Fmoc-Phe. The fibres appear rather straight on prG and curvy on oxG. Supported by DFT calculations, the self-assembly of amphiphilic Fmoc-Phe is a surface-mediated process, *i.e.*, the self-assembly process starts from the first layer of molecules adsorbed on the surface.

In addition, the Fmoc-Phe gel on prG consists of a heterogeneous network, as observed at a single fibre level. Our results are in accordance with previous findings on polymorphism in Fmoc-Phe bulk gels. However, we prove that the heterogeneity of the secondary organization level initiates at the nanoscale. It is of note that the presented observations reflect the experimental conditions and may change under different conditions (*i.e.*, different solvents, Fmoc-Phe concentration, or sample volume).

In future, the surface effects on the physical properties of the wet gel remain to be studied. We believe that a thorough understanding of the interactions between a surface and an ECM-biomimetic gel is crucial for the engineering of bioelectronic interfaces, towards next-generation neuron–machine connections.

Author contributions

J. S.: investigation; formal analysis; validation; writing – original draft, review & editing. R. C., A. E., E. H.: investigation;

writing – review & editing. A. J.: investigation. P. M.: design and development of the oxidation laser setup. M. N., E. D. S.: conceptualization; supervision; writing – review & editing. M. P.: funding acquisition; project administration; supervision; writing – review & editing.

Conflicts of interest

There are no conflicts to declare.

Acknowledgements

References

1 M. Bramini, G. Alberini, E. Colombo, M. Chiacchiaretta, M. L. DiFrancesco, J. F. Maya-Vetencourt, L. Maragliano, F. Benfenati and F. Cesca, *Front. Syst. Neurosci.*, 2018, **12**, 12.

2 A. B. Rapeaux and T. G. Constandinou, *Curr. Opin. Biotechnol*, 2021, **72**, 102–111.

3 S. R. Shin, Y. C. Li, H. L. Jang, P. Khoshakhlagh, M. Akbari, A. Nasajpour, Y. S. Zhang, A. Tamayol and A. Khademhosseini, *Adv. Drug Delivery Rev.*, 2016, **105**, 255–274.

4 N. Wu, S. Wan, S. Su, H. Huang, G. Dou and L. Sun, *InfoMat*, 2021, **3**, 1174–1194.

5 A. K. Geim and K. S. Novoselov, *Nat. Mater.*, 2007, **6**, 183–191.

6 C. Hébert, E. Masvidal-Codina, A. Suarez-Perez, A. B. Calia, G. Piret, R. Garcia-Cortadella, X. Illa, E. del Corro Garcia, J. M. de la Cruz Sanchez, D. V. Casals, E. Prats-Alfonso, J. Bousquet, P. Godignon, B. Yvert, R. Villa, M. V. Sanchez-Vives, A. Guimerà-Brunet and J. A. Garrido, *Adv. Funct. Mater.*, 2018, **28**, 1703976.

7 C. Lee, X. Wei, J. W. Kysar and J. Hone, *Science*, 2008, **321**, 385–388.

8 J. Aumanen, A. Johansson, J. Koivistoinen, P. Myllyperkiö and M. Pettersson, *Nanoscale*, 2015, **7**, 2851–2855.

9 E. D. Sitsanidis, J. Schirmer, A. Lampinen, K. K. Mentel, V. M. Hiltunen, V. Ruokolainen, A. Johansson, P. Myllyperkiö, M. Nissinen and M. Pettersson, *Nanoscale Adv.*, 2021, **3**, 2065–2074.

10 A. Johansson, H.-C. Tsai, J. Aumanen, J. Koivistoinen, P. Myllyperkiö, Y.-Z. Hung, M.-C. Chuang, C.-H. Chen, W. Y. Woon and M. Pettersson, *Carbon*, 2017, **115**, 77–82.

11 B. Alberts, A. Johnson, J. Lewis, D. Morgan, M. Raff and K. Roberts, *Molecular Biology of the Cell*, Garland Science, 6th edn, 2015, pp. 1035–1090.

12 P. C. Georges, W. J. Miller, D. F. Meaney, E. S. Sawyer and P. A. Janmey, *Biophys. J.*, 2006, **90**, 3012–3018.

13 J. Lantoine, T. Grevesse, A. Villers, G. Delhaye, C. Mestdagh, M. Versaevel, D. Mohammed, C. Bruyère, L. Alaimo, S. P. Lacour, L. Ris and S. Gabriele, *Biomaterials*, 2016, **89**, 14–24.

14 S. Sur, C. J. Newcomb, M. J. Webber and S. I. Stupp, *Biomaterials*, 2013, **34**, 4749–4757.

15 E. R. Draper and D. J. Adams, *Chem*, 2017, **3**, 390–410.

16 L. A. Estroff and A. D. Hamilton, *Chem. Rev.*, 2004, **104**, 1201–1217.

17 B. A. Simmons, C. E. Taylor, F. A. Landis, V. T. John, G. L. McPherson, D. K. Schwartz and R. Moore, *J. Am. Chem. Soc.*, 2001, **123**, 2414–2421.

18 E. Mayans and C. Alemán, *Molecules*, 2020, **25**, 6037.

19 D. M. Murali and G. Shanmugam, *New J. Chem.*, 2019, **43**, 12396–12409.

20 V. Singh, K. Snigdha, C. Singh, N. Sinha and A. K. Thakur, *Soft Matter*, 2015, **11**, 5353–5364.

21 M. G. F. Angelerou, A. Sabri, R. Creasey, P. Angelerou, M. Marlow and M. Zelzer, *Chem. Commun.*, 2016, **52**, 4298–4300.

22 M. G. F. Angelerou, B. Yang, T. Arnold, J. Rawle, M. Marlow and M. Zelzer, *Soft Matter*, 2018, **14**, 9851–9855.

23 M. Criado-Gonzalez, M. H. Iqbal, A. Carvalho, M. Schmutz, L. Jierry, P. Schaaf and F. Boulmedais, *Front. Bioeng. Biotechnol.*, 2020, **8**, 938.

24 V. V. Korolkov, S. Allen, C. J. Roberts and S. J. B. Tendler, *Faraday Discuss.*, 2013, **166**, 257–267.

25 B. Yang, M. Lledos, R. Akhtar, G. Ciccone, L. Jiang, E. Russo, S. Rajput, C. Jin, M. G. F. Angelereou, T. Arnold, J. Rawle, M. Vassalli, M. Marlow, D. J. Adams and M. Zelzer, *Chem. Sci.*, 2021, **12**, 14260–14269.

26 A. Accardo, V. Shalabaeva, E. di Cola, M. Burghammer, R. Krahne, C. Riekel and S. Dante, *ACS Appl. Mater. Interfaces*, 2015, **7**, 20875–20884.

27 M. Mahmoudi, O. Akhavan, M. Ghavami, F. Rezaee and S. M. A. Ghiasi, *Nanoscale*, 2012, **4**, 7322–7325.

28 K. Shezad, K. Zhang, M. Hussain, H. Dong, C. He, X. Gong, X. Xie, J. Zhu and L. Shen, *Langmuir*, 2016, **32**, 8238–8244.

29 A. Keller, M. Fritzsche, Y. P. Yu, Q. Liu, Y. M. Li, M. Dong and F. Besenbacher, *ACS Nano*, 2011, **5**, 2770–2778.

30 I. Amenabar, S. Poly, W. Nuansing, E. H. Hubrich, A. A. Govyadinov, F. Huth, R. Krutokhvostov, L. Zhang, M. Knez, J. Heberle, A. M. Bittner and R. Hillenbrand, *Nat. Commun.*, 2013, **4**, 2890.

31 F. Huth, A. Govyadinov, S. Amarie, W. Nuansing, F. Keilmann and R. Hillenbrand, *Nano Lett.*, 2012, **12**, 3973–3978.

32 M. Paulite, Z. Fakhraai, I. T. S. Li, N. Gunari, A. E. Tanur and G. C. Walker, *J. Am. Chem. Soc.*, 2011, **133**, 7376–7383.

33 T. Taubner, R. Hillenbrand and F. Keilmann, *Appl. Phys. Lett.*, 2004, **85**, 5064–5066.

34 X. Ma, Q. Liu, N. Yu, D. Xu, S. Kim, Z. Liu, K. Jiang, B. M. Wong, R. Yan and M. Liu, *Nat. Commun.*, 2021, **12**, 6868.

35 S. Kim, N. Yu, X. Ma, Y. Zhu, Q. Liu, M. Liu and R. Yan, *Nat. Photon*, 2019, **13**, 636–643.

8732 | *Phys. Chem. Chem. Phys.*, 2023, **25**, 8725–8733

This journal is © the Owner Societies 2023

36 J. Lee, K. T. Crampton, N. Tallarida and V. A. Apkarian, *Nature*, 2019, **568**, 78–82.

37 A. Y. Gahane, P. Ranjan, V. Singh, R. K. Sharma, N. Sinha, M. Sharma, R. Chaudhry and A. K. Thakur, *Soft Matter*, 2018, **14**, 2234–2244.

38 A. Rajbhandary, W. W. Brennessel and B. L. Nilsson, *Cryst. Growth Des.*, 2018, **18**, 623–632.

39 D. M. Ryan, S. B. Anderson and B. L. Nilsson, *Soft Matter*, 2010, **6**, 3220–3231.

40 B. Adhikari, G. Palui and A. Banerjee, *Soft Matter*, 2009, **5**, 3452–3460.

41 A. M. Smith, R. J. Williams, C. Tang, P. Coppo, R. F. Collins, M. L. Turner, A. Saiani and R. V. Ulijn, *Adv. Mater.*, 2008, **20**, 37–41.

42 D. Giuri, L. J. Marshall, C. Wilson, A. Seddon and D. J. Adams, *Soft Matter*, 2021, **17**, 7221–7226.

43 E. S. Gadelmawla, M. M. Koura, T. M. A. Maksoud, I. M. Elewa and H. H. Soliman, *J. Mater. Process. Technol.*, 2002, **123**, 133–145.

44 E. R. Draper, K. L. Morris, M. A. Little, J. Raeburn, C. Colquhoun, E. R. Cross, T. O. McDonald, L. C. Serpell and D. J. Adams, *CrystEngComm*, 2015, **17**, 8047–8057.

45 A. Barth, *Biochim. Biophys. Acta*, 2007, **1767**, 1073–1101.

46 A. Barth and C. Zscherp, *Q. Rev. Biophys.*, 2002, **35**, 369–430.

47 S. Mastel, A. A. Govyadinov, T. V. A. G. de Oliveira, I. Amenabar and R. Hillenbrand, *Appl. Phys. Lett.*, 2015, **106**, 023113.

48 H. Wang, L. Wang, D. S. Jakob and X. G. Xu, *AIP Adv.*, 2017, **7**, 055118.

49 A. Barth, *Prog. Biophys. Mol. Biol.*, 2000, **74**, 141–173.

50 X. Liu, *Organic Chemistry I*, Kwantlen Polytechnic University, 2021, pp. 197–200.

This journal is © the Owner Societies 2023

Phys. Chem. Chem. Phys., 2023, **25**, 8725–8733 | 8733